Mechanics of Time-Dependent Materials (2026) 30:12
https://doi.org/10.1007/s11043-026-09855-7

RESEARCH

Modelling of viscoplastic properties of epoxy resins in fibre-reinforced unidirectional composites

Vincent Feyen[1] · Christian Breite[1] · Jérémy Chevalier[2] · Thomas Pardoen[2,3] · Yentl Swolfs[1]

Received: 14 July 2025 / Accepted: 20 January 2026
© The Author(s), under exclusive licence to Springer Nature B.V. 2026

Abstract
Accurate prediction of the lifetime of unidirectional fibre composites requires a model that captures matrix viscoplasticity across generic loading histories. We propose a compact, rate-dependent hardening law for highly crosslinked epoxies that unifies constant-strain-rate and creep behaviour. The yield stress depends exponentially on accumulated plastic strain and logarithmically on plastic strain rate, and the relationship is analytically invertible for direct use in a finite element code. Parameters are calibrated from compression tests at multiple strain rates and from hold-at-load creep tests; validation is performed on RTM-6 and new 736LT epoxy data. The model reproduces (i) the near-linear σ_y–$\log \dot{\varepsilon}$ trend from pre-yield through softening and hardening, (ii) the time-dependent transition from pre- to post-yield during creep, including the rate surge near softening, (iii) long-term (14.5 h) creep more faithfully than stress–time power laws, and (iv) trends in cyclic, variable-rate, and tensile tests. The resulting, easily calibrated formulation enables robust simulation of matrix viscoplasticity in composite-scale models, improving durability predictions for load-bearing structures such as pressure vessels and wind-turbine blades.

Keywords Viscoplastic behaviour · Epoxy resin composites · Time-dependent constitutive modelling · Long-term load performance · Creep compression testing

1 Introduction

Time-dependent failure of composites often plays a major role in the design of any statically loaded component, for example, in the service life of composite pressure vessels (Mair 2017). The degradation of composite materials over time is not always clear since the overall strain or appearance does not change significantly, while internal damage can grow over time

✉ Y. Swolfs
yentl.swolfs@kuleuven.be

1 Department of Materials Engineering, Faculty of Engineering, KU Leuven, Kasteelpark Arenberg 44, Leuven, 3001, Belgium

2 Department of Mechanics, Materials and Civil Engineering (iMMC), UCLouvain, Place Sainte Barbe 2, Louvain-la-Neuve, 1348, Belgium

3 WEL Research Institute, Avenue Pasteur 6, Wavre, 1301, Belgium

Published online: 27 January 2026

(Cole et al. 2017). Insufficient knowledge of the failure mechanism can lead to large safety factors or frequent maintenance inspections. Measuring the residual properties and degradation of a composite over time is a complex matter due to the many influencing factors and the existence of complex damage modes. Modelling this time-dependent degradation is essential, as it could yield important insights into the mechanisms and estimate the lifetime under a given load. It is generally accepted that the final failure of composite materials is caused by fibre failure when loaded in tension. Previous studies show that failure develops in different stages. First, the weakest fibres break at a certain strain because the fibre strength follows a weakest link or Weibull distribution based on defects in the fibres (Rosen 1964; Kelly and Barbero 1993; Schadler et al. 1996). These breaks are spread out across the whole volume of a ply (Phoenix et al. 1988). When a fibre breaks, its load is distributed to the neighbouring intact fibres. The matrix transfers this load via shear stress from the broken fibre to the neighbouring ones (Schadler et al. 1996; Lagoudas et al. 1989). This results in an overload of the neighbouring fibres, increasing their failure probability and causing a tendency to form clusters (Thionnet et al. 2014; Scott et al. 2011). This process will continue until one cluster becomes critical and will catalyse the final composite failure.

The time dependency of longitudinal tensile failure is most often attributed to the viscous properties of the matrix (Phoenix et al. 1988; Thionnet et al. 2014; Lifshitz and Rotem 1970; Kumar and Talreja 2003; Perreux and Thiebaud 2011). When the matrix is stressed after an initial fibre break, it relaxes over time, inducing an increased ineffective length and spreading the overload to a larger portion of the neighbouring fibres (Rosen 1964; Lifshitz and Rotem 1970; Iyengar and Curtin 1997; Du and McMeeking 1985; Miyake 2011). The probability of creating new fibre breaks near existing ones will increase over time until one cluster becomes critical, leading to final failure. The time required to develop such a cluster will determine the lifetime of the composite under this given load condition.

The time-dependent parameters are sometimes extracted from a low-load tensile test or an in-situ stress measurement using micro-Raman spectroscopy. The in-situ approach is conducted on a 2D unidirectional (UD) composite specimen or the surface of a 3D one held at a constant macroscopic displacement. The fibre stress is calculated by measuring the change of a calibrated Raman shift (Miyake 2011; Beyerlein et al. 2003; Zhou et al. 2003). However, the accuracy of such measurements seems to be limited. Extracting the time-dependent properties is non-trivial, and the loading conditions are different than those in the centre of a 3D closely packed composite. Note that the time-dependent viscoplastic response of the epoxy matrix plays a role under creep-type loading conditions, such as around bolted areas, under cyclic loadings, especially at moderate temperatures, or under high-rate transverse loading problems.

The failure of a bulk epoxy specimen strongly depends on the loading condition. When performing a tensile test, the epoxy behaves in a brittle manner; it behaves almost linearly elastic up to the point of instantaneous rupture (Hsieh et al. 2010; Hobbiebrunken et al. 2007; Kontou 2011; Silva et al. 2017). No damage or plasticity was observed before this point (Lifshitz and Rotem 1970; Morelle 2015). When loaded in compression, the behaviour changes significantly. The material exhibits significant non-linear elastoplastic behaviour up to the upper yield stress σ_u, followed by softening and hardening up to 70% true strain as depicted in Fig. 1 (Hsieh et al. 2010; Morelle 2015; Costa Mattos 2013; Foreman et al. 2008; Jianlin et al. 2022; Kumar et al. 2024; Liu et al. 2022). Recent studies on thin epoxy fibres indicated similar plastic behaviour in tension (Hobbiebrunken et al. 2007; Misumi et al. 2016; Sui et al. 2019; Verschatse et al. 2020). Chevalier et al. (2016) investigated this size effect and concluded that this limiting strength in tension corresponds to reaching the maximum theoretical principal stress inside the resin at a submicrometre defect with a

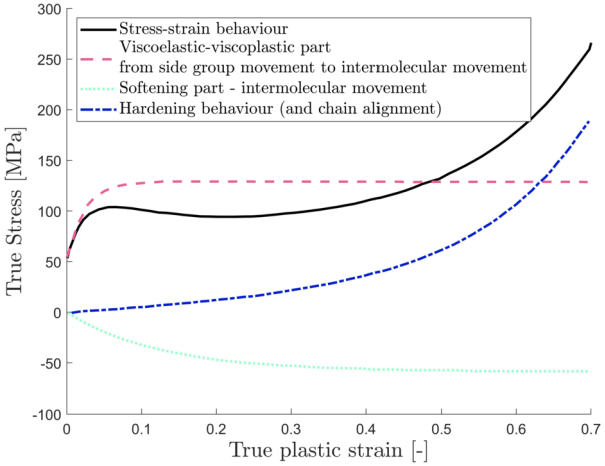


Fig. 1 Contributions to the epoxy compression behaviour (adapted from Morelle et al. 2017, with permission from Springer) (Color figure online)

critical aspect ratio. Using molecular dynamics simulations (Neogi 2018) and experimental double-notch tests (Rojek et al. 2020), one possible submicrometer defect was identified to be a void, which can grow over time under a tensile load. One could assume that a resin pocket near a fibre break has a low probability of exhibiting such a defect due to its limited size and should thus be characterised by its full non-linear elastoplastic behaviour (Heuvel et al. 1998). Moreover, the stress near a fibre break is mainly shear stress, which leads to a large deformation rather than fracture (Fiedler et al. 2001).

Modelling strategies for the time-dependent behaviour of epoxy resins vary considerably. Most studies rely on empirical power-law formulations, expressed as a function of time (Phoenix et al. 1988; Lagoudas et al. 1989; Perreux and Thiebaud 2011; Beyerlein et al. 1998, 2003; Kotelnikova-Weiler et al. 2017; Koyanagi et al. 2007; Zhou et al. 2002; Feng et al. 2005), stress state (Iyengar and Curtin 1997; Ohno and Miyake 1999; Liu et al. 2022), (plastic) strain state (Du and McMeeking 1985; Jianlin et al. 2022), or combinations thereof (Kelly and Barbero 1993; Okabe et al. 2010; Goertzen and Kessler 2006; Mason et al. 1992; Paul and Singh 2022). Other approaches describe creep or relaxation behaviour through time-dependent compliance (Lifshitz and Rotem 1970; Krauklis et al. 2019), apparent shear relaxation moduli (Nakada and Miyano 2013), or classical spring–dashpot analogues such as Zener or Burgers-type models (Blassiau et al. 2006; Nechad et al. 2005; Paul and Singh 2022; Liu et al. 2022; Kumar et al. 2024; Gerritzen et al. 2022; Nguyen et al. 2016; Zhang et al. 2022; Ilioni et al. 2018). However, these last models are generally limited to the viscoelastic regime well below the yield point and do not adequately capture the transition from pre-yield to post-yield behaviour. To the best of the authors' knowledge, no continuum-level model has yet been published that captures the creep behaviour across this transition and into the softening region after the yield point. The notable exception is the mesoscale model by Chevalier et al. (2018), which explicitly considers Shear Transformation Zones (STZs). While physically insightful, such mesoscale descriptions are not readily applicable in macroscopic finite element simulations. Since the local shear stress near fibre breaks can exceed the epoxy yield strength, capturing the full creep response—from pre-yield to post-yield—is essential for accurate lifetime prediction of fibre-reinforced composites.

The aim of this study is therefore to develop a novel, rate-dependent hardening law capable of describing both the instantaneous and time-dependent mechanical behaviour of highly crosslinked epoxies. Building on previous findings for the RTM-6 resin system, the

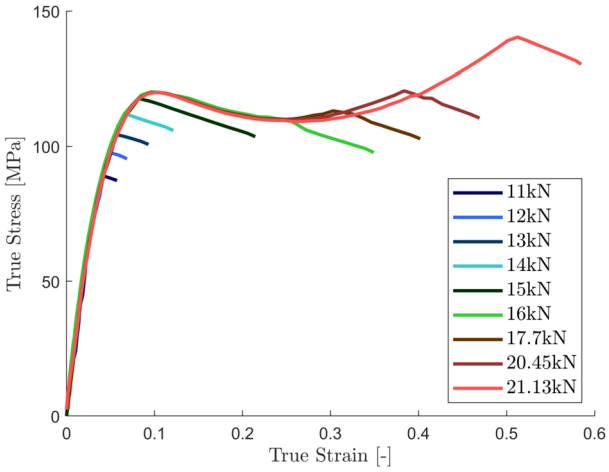


Fig. 2 Creep tests at different load levels (11.00 - 21.13 kN) performed at different levels of strain on the RTM-6 resin, the holding time was 2000 seconds (adapted from Morelle 2015 with permission from the author)(Color figure online)

proposed phenomenological law is validated using new experimental data for the 736LT epoxy resin. Owing to its simplicity and closed-form nature, the model can be implemented efficiently into finite element software (here, Abaqus FEA). The parameters are calibrated using simple compressive constant-strain-rate tests and hold-at-load creep experiments on macroscopic cylindrical epoxy specimens. The model is then assessed under various loading conditions, including long-term creep, cyclic loading, tension, and variable strain-rate tests. A key contribution of this work is to demonstrate that both moderate-rate and quasi-static creep behaviour can be unified under a single hardening law, reflecting a common underlying mechanism. The model, supported by experimental results, predicts a time-dependent transition from the pre-yield to post-yield regime—marked by pronounced plastic deformation—which governs the stress redistribution in the matrix near fibre breaks and therefore plays a central role in the long-term failure of fibre-reinforced composites.

2 Rate-dependent hardening law

The formulation of the hardening law is based on the work by Morelle and co-authors (Morelle 2015; Morelle et al. 2017) on the highly crosslinked RTM-6 resin. Morelle took into account three contributions to the specific non-linear elastoplastic behaviour: a non-linear viscoelastic-viscoplastic contribution, a softening regime, and the hardening part (see Fig. 1). Exponential empirical functions were proposed to represent both the first two contributions. The hardening part was modelled by an inverse Langevin function. The reader is referred to (Morelle et al. 2017) for more details on this static model. The variation of the yield stress of the RTM-6 resin in compression determined at a constant strain rate was found to depend linearly on the logarithm of the strain rate (Morelle et al. 2017). Morelle conducted various hold-at-constant-load creep tests as well, in which a cylindrical epoxy specimen was compressed up to a certain strain, after which it was held at a constant load for 2000 s (Morelle 2015). Figure 2 summarises the results. The creep strain depends not only on stress but also on the overall strain imposed prior to the creep step. The creep rate is significantly higher in the softening stage compared to the hardening regime, whilst creep is much slower in the pre-yield region.

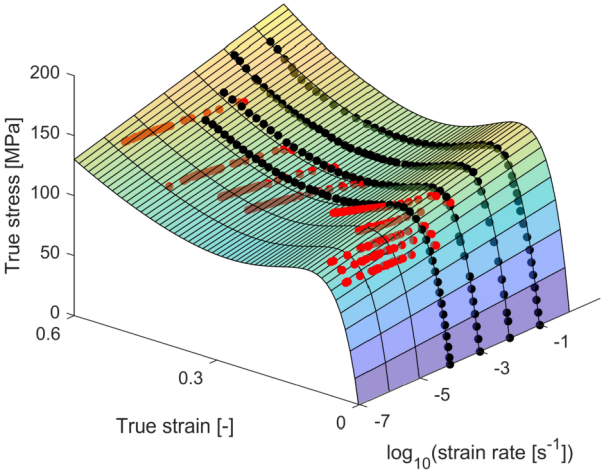


Fig. 3 Hold-at-constant-load and constant strain rate data are combined in one figure for the RTM-6 resin. The data used in this plot was obtained from the work of Morelle (2015) (Color figure online)

If the mechanisms of plastic deformation in a constant strain rate and creep test are the same, one could assume that an adequate viscoplastic hardening law should be able to encompass both phenomena as a manifestation of a single underlying more fundamental viscoplastic deformation mechanism, such as suggested for instance by Chevalier et al. (2018) based on a molecular informed shear transformation zone model. Indeed, one can observe, and this is a key novel element of the analysis of this study, such a similarity when gathering all data in a unique stress-strain-strain rate diagram depicted in Fig. 3. The hold-at-constant-load tests contain information on the material behaviour at very low strain rates, complementary to the moderate to high strain rate data of the constant strain rate tests. Moreover, the strain rate dependency appears linear on a logarithmic scale, even at low strain rates.

Based on this empirical observation, the following hardening law for the yield stress is proposed, using the classical separation of total strain into elastic and plastic strain ($\varepsilon_t = \varepsilon_e + \varepsilon_p$):

$$\begin{aligned}\sigma_y = &\left(C_1 \log_{10} \dot{\varepsilon}_p + C_2\right) \exp(-C_3 \varepsilon_p) - \left(C_4 \log_{10} \dot{\varepsilon}_p + C_5\right) \exp(-C_6 \varepsilon_p) \\ &+ \left(C_7 \log_{10} \dot{\varepsilon}_p + C_8\right) \exp(C_9 \varepsilon_p).\end{aligned} \tag{1}$$

in which σ_y is the true yield stress, $\dot{\varepsilon}_p$ the true plastic strain rate, ε_p the true plastic strain, and $C_{1,\ldots,9}$ positive empirical coefficients. The coefficients can be identified based on several experiments. The yield stress equation contains three terms based on Morelle et al. (2017): the non-linear viscoplastic, the softening, and the hardening contribution, represented by exponential functions. The logarithmic strain rate dependency is added in the pre-factor for each of the three terms. This equation is purely empirical but exhibits a very useful property from a modelling perspective: it can be inverted with respect to strain rate. One can rearrange Equation (1) into an analytical equation for the plastic strain rate as a function of the true stress and plastic strain:

$$\log_{10} \dot{\varepsilon}_p = \frac{\sigma_y - C_2 \exp(-C_3 \varepsilon_p) + C_5 \exp(-C_6 \varepsilon_p) - C_8 \exp(C_9 \varepsilon_p)}{C_1 \exp(-C_3 \varepsilon_p) - C_4 \exp(-C_6 \varepsilon_p) + C_7 \exp(C_9 \varepsilon_p)}. \tag{2}$$

Equation (2) can also be differentiated with respect to stress and strain. When implemented in an implicit finite element (FE) solver with the relevant plasticity theory (in this case,

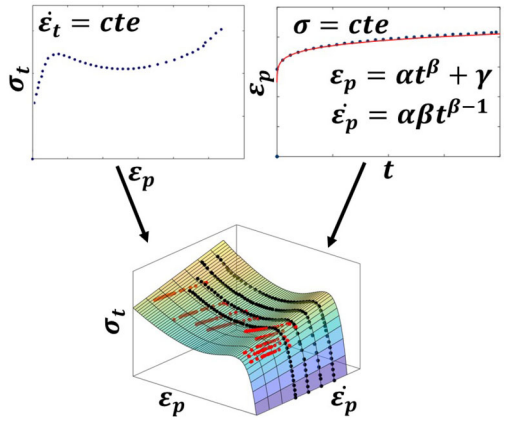


Fig. 4 A fitting scheme is used to obtain the coefficients of the constitutive law from the hold-at-load and constant strain rate data. The data used for illustration purposes in this plot was obtained from the work of Morelle (2015) (Color figure online)

Abaqus (Smith 2009)), these values are required to improve convergence, allowing for larger time steps (Systemes 2023). Another advantage of this equation is that it can reproduce the softening part (see Fig. 1) of the stress-strain diagram without encountering convergence issues.

The empirical coefficients in Equation (1) are obtained based on two types of experiments, the constant strain rate compression test and the hold-at-load compression creep tests. In the latter test, the plastic strain is fitted as a function of time, for each individual sample, with a simple power law:

$$\varepsilon_p = \alpha t^{\beta} + \gamma. \tag{3}$$

Hereafter, the instantaneous strain rate is calculated based on the derivative of Equation (3) with respect to time. Finally, all data points can be plotted into a single three-dimensional plot, displaying the true stress as a function of true plastic strain and true plastic strain rate for both the constant strain rate tests and the hold-at-load tests. The fitting of Equation (1) was conducted using the Matlab fitting toolbox. The fitting scheme is depicted in Fig. 4. For more details, the reader is referred to the automated script and the raw data files available to download from Mendeley data (Feyen et al. 2024).

The RTM-6 resin demonstrates complex non-linear unloading behaviour, identified by Chevalier et al. to be caused by back stresses in the material (Chevalier et al. 2018). The proposed model does not consider these back stresses and accounts solely for linear elasticity and plasticity governed by the proposed hardening law (see Equation (1)).

Morelle et al. (2017) used a Drucker-Prager constitutive model to account for the asymmetry in yield behaviour. In their work, the yield stress in tension was 86% of that in compression, displaying a moderate asymmetry. In practice, tensile and shear deformation tests should be conducted up to large strains to assess this asymmetry. This asymmetry was not taken into account due to the uncertainty of the post-yield behaviour, and for the sake of simplicity, J2 plasticity was selected, relying on the isotropic von Mises yield locus. Further experimental tests using small-scale specimens should be conducted to enable the model to account for possible asymmetry (Hobbiebrunken et al. 2007; Misumi et al. 2016; Littell et al. 2008).

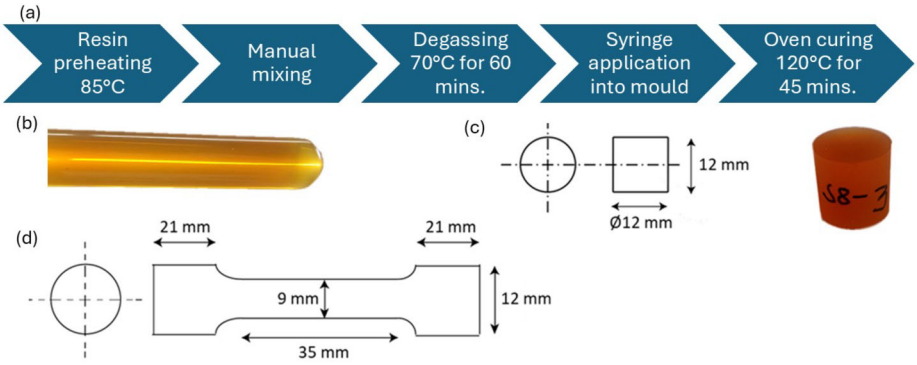


Fig. 5 (a) the workflow of the tensile and compression specimens processing from resin to cylindrical slab, (b) the demoulded cylindrical slab, (c) dimensions of the compression test sample, and (d) dimensions of the tensile test sample (Color figure online)

3 Materials and methods

3.1 Materials and production

The material investigated in this study is the 736LT epoxy resin, which is used for the production of thin-ply pre-impregnated (prepreg) by North Thin Ply Technology (NTPT). The manufacturer of the 736LT resin supplied the datasheet for the prepreg material, which did not contain detailed information on the mechanical properties of the resin (NTPT Thinpreg 736LT Datasheet 2017). The epoxy resin was supplied as two components: base resin (bisphenol-A type) and hardener (amine). The epoxy was prepared using 26 parts of hardener to 100 parts of resin, based on correspondence with the manufacturer. At room temperature, the resin is too viscous (1 × 105 Pa.s) to be moulded, so it was pre-heated to 85 °C. The pre-heating was followed by manual mixing with the hardener using a spatula to avoid air entrapment commonly observed when using electric mixers. Degassing was conducted at 70 °C in a vacuum oven (Vacutherm, Heraeus instruments) for a period of 60 minutes to remove entrapped volatiles. A syringe with a large diameter nozzle was used to pour the resin into cylindrical test tubes of 16 mm diameter and 100 mm length. The tubes were treated with Chemlease® PMR 90 EZ release agent before pouring in the resin. The prepared test tubes were placed in a holder to facilitate the airflow in a convection oven (Memmert UF 110) and guarantee an even temperature distribution. A stepwise temperature increase was used to cure the mixed epoxy resin, according to the manufacturer (NTPT Thinpreg 736LT Datasheet 2017). The full workflow of the resin production process is depicted in Fig. 5a. The obtained cylindrical slabs did not contain macroscopic voids or porosities. A slight colour gradient was present at the top and bottom (see Fig. 5b), but these areas were removed during machining. From the cylindrical slabs, cylindrical compression specimens were machined according to dimensions based on the ASTM D695 standard with a height of 12 mm and a diameter of 12 mm (ASTM 2015) (see Fig. 5c). Cylindrical dumbbell-shaped specimens were machined for uniaxial tensile testing with a 9 mm diameter and a 35 mm gauge length (see Fig. 5d).

3.2 Constant strain rate tests

Compression tests were conducted using a dedicated fixture described in the ASTM D695, produced by Wyoming Test Fixtures Inc. (WTF-SP 1” diameter). The tests were conducted

on a Zwick/Roell Z250 with a central ball-lead screw and a load cell of 30 kN. The ambient temperature was controlled at 23 °C with a relative humidity of 40%. A polytetrafluoroethylene (PTFE) film with a thickness of 70 μm was placed at the top and bottom of the specimen to avoid barrelling, as suggested by (Chevalier et al. 2016; Morelle et al. 2017). During the tests, only slight amounts of barrelling developed at the highest strain levels. Some specimens deformed slightly in shear, possibly caused by the friction between the specimen and fixture being too low. These were excluded from the dataset when the shear deformation was deemed significant. The extracted displacement data was corrected for machine compliance, which was measured separately by using the fixture without a specimen present to obtain the force-displacement curve. Four quasi-true strain rate tests were performed, namely 0.1 s^{-1}, 0.01 s^{-1}, 0.001 s^{-1}, and 0.0001 s^{-1}. The quasi-true strain rate was estimated by assuming perfect plasticity (volume conservation) and by using the dimensions and geometry of the undeformed specimens.

3.3 Hold-at-load tests

The hold-at-load tests were conducted in compression to avoid premature failure at pre-existing defects (Chevalier et al. 2016). The same setup and climatic conditions as described in Sect. 3.1 were used. The specimen was loaded to a predefined strain at a constant strain rate of 0.001 s^{-1}, after which the load was held constant for 2000 s, followed by unloading at the same rate, similar to the procedure applied on the RTM-6 resin (Morelle 2015). Specimens were held at six different load levels in the pre-yield region (1.1, 3.4, 5.6, 7.9, 10.2, and 11.3 kN) and three in the post-yield region (12.4, 17, and 23 kN). An overnight hold-at-load test was conducted to examine the validity of extrapolating the constitutive model based on short-term hold-at-load data (2000 s) and constant strain rate data towards longer timescales. The specimen was compressed for over 14.5 hours (52200 s) under a load of 11.5 kN, just below the upper yield stress. This load was chosen to capture the transition between pre-yield and post-yield creep behaviour within the test time.

3.4 Strain rate jump tests

A strain rate jump test was performed in compression using the same setup described in Sect. 3.1. During the test, the cross-head displacement rate was abruptly increased from 0.1 to 1, 10, and 100 mm/min at macroscopic true strains of 0.15, 0.27, and 0.41 for the RTM-6 resin (Morelle 2015), and at 0.15, 0.41, and 0.64 for the 736LT resin tested in this work. The 736LT resin exhibited larger ductility than the RTM-6 resin; therefore, the strain intervals for the rate jumps were distributed more evenly across the higher strain range.

3.5 Cyclic loading tests

One cyclic loading test was conducted in compression using a similar setup and climatic conditions described in Sect. 3.1. The cross-head velocity was set at 0.1 mm/min. The specimen was compressed up to a true strain of 0.088, after which it was unloaded at the same rate. This was followed by a reloading step and unloading at true strains of 0.2, 0.28, 0.38 and 0.49 for the RTM-6 resin (Morelle 2015) and at 0.067, 0.18, 0.32, 0.46, and 0.61 for the 736LT resin, performed in this work, respectively.

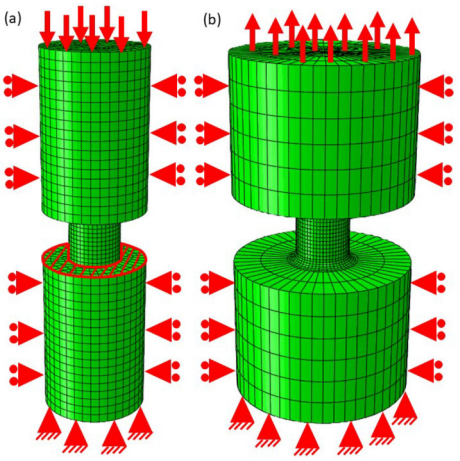


Fig. 6 FEM of (a) an epoxy cylinder in between two steel holders and (b) the tensile specimen (Color figure online)

3.6 Uniaxial tensile test

An uniaxial tensile test was conducted to assess the validity of extending the epoxy model towards tensile behaviour. The specimens were tested on an Instron 5567 universal testing machine with a 30 kN load cell. The constant cross-head displacement was set to obtain a true strain rate of 0.001 s^{-1}. The tensile specimens were speckled using a black-and-white pattern to obtain high-contrast points. Digital-Image-Correlation (DIC) was used to monitor the in-situ 2D true strain using the Limess Vic2D-2009 software package. The measured load was directly used as input for the DIC software to ensure accurate data synchronisation.

3.7 Finite element modelling procedures

A finite element model (FEM) was executed using Abaqus 2023 CAE commercial software from Simulia/Dassault Systèmes, in conjunction with a FORTRAN compiler (Intel C++ 2018 and Intel Fortran 2018), to validate the fitting procedure and assess the applicability of the novel treatment of rate-dependent hardening. All scripts and models used in this study are available to download from Mendeley data (Feyen et al. 2024). The epoxy cylinder was simulated under both compression and tension, with the boundary conditions and loads illustrated in Fig. 6. Although the current loading configurations for the resin are axisymmetric, 3D simulations were conducted to showcase the numerical efficiency and robustness of the model.

In the compression model (see Fig. 6a), the top of the upper cylinder was subjected to a displacement or pressure boundary condition to compress the specimen, accompanied by an additional boundary condition to constrain its in-plane movement. The bottom of the lower cylinder was fully constrained, and all other free surfaces were left unconstrained. A surface-to-surface contact boundary condition was applied between the steel cylinders (master) and the epoxy cylinder (slave), allowing the surfaces to slide over one another. A default friction coefficient of 0.01 was used. Simulations using a friction coefficient of 0.1 were conducted to examine the effect of friction on the apparent stress-strain behaviour for different loading conditions. When friction is present, the specimen exhibits some barrelling, which is more pronounced at higher deformations. The latter was also observed experimentally. The stress state within the material is no longer uniform at this point. The overall external work

combined with the displacement of the top cylinder, was used to generate the yield curve, assuming perfect plastic homogeneous deformation (similar to what one assumes when extracting the experimental test data), to avoid the ambiguity of the non-uniform stress state. The cylinders representing the test fixture were modelled as elastic, with a modulus of 800 GPa to ensure minimum deformation (and thus energy increase in the simulation model), thereby neglecting machine compliance. Note that all the experimental results are corrected for this compliance separately. The tensile sample (see Fig. 6b) was modelled as a cylindrical specimen with an increased surface area near the ends to obtain a uniform uniaxial tensile stress in the central part. The advantage of this setup is that a constant load can be applied as a constant pressure boundary condition at the upper face of the model while avoiding tedious contact constraints when using separate steel cylinders to obtain a similar effect. The matrix behaviour was modelled to be linear elastic-viscoplastic using the Abaqus CREEP subroutine, written in FORTRAN (provided in Feyen et al. 2024). In this subroutine, the deformation of the matrix is controlled by the equivalent plastic strain and true stress in the element, as explained in the Abaqus User Subroutines Reference Guide (Systemes 2023). The hardening law and its derivatives need to be defined by the user and were obtained using Equation (1). Several different simulations were conducted using this model. First and foremost, the hold-at-load and constant strain rate tests were replicated to evaluate the accuracy of the calibration procedure, both for the 736LT resin and the RTM-6 resin. The test data of the RTM-6 resin was used from the work of Morelle (2015). Next, three simulations mimicking the different loading conditions (cyclic, variational strain rate and tensile) of the validation tests were computed to assess the limitations and validity of the model. Additionally, the extrapolation of the creep data towards larger timescales was investigated, and a comparison was made between the time-dependent power law, most often used in the literature (Kelly and Barbero 1993; Phoenix et al. 1988; Lagoudas et al. 1989; Beyerlein et al. 1998; Kotelnikova-Weiler et al. 2017; Koyanagi et al. 2007; Zhou et al. 2002; Goertzen and Kessler 2006; Mason et al. 1992), and the current model for the overnight hold-at-constant-load test (14.5 hours). The power law was fitted with a stress dependency in the pre-yield region, using the same experimental data for the RTM-6 and the 736LT resin. Finally, a simulation of a creep test in tension was conducted to examine whether the model captures the three classical creep stages (primary, secondary, and tertiary creep (Nechad et al. 2005; Vujosevic and Krajcinovic 1997)).

4 Results and discussion: experiments and simulations

The datasets from the constant strain rate and hold-at-load tests were combined, and the fitting procedure described in Sect. 2 was applied to both the 736LT resin (using the experiments performed in this work) and the RTM-6 resin (using the data of Morelle 2015). The constants of the proposed hardening law are provided in the accompanying Fortran subroutine files (Feyen et al. 2024). Conversion of the load-displacement curves to true stress–true strain curves was performed under the assumption of homogeneous deformation. At high loads, however, the specimens exhibited noticeable barreling, violating this assumption and reducing the reliability of the curves in the large strain range. Nevertheless, a consistent comparison between experiments and simulations remains valid, as the mechanism of barreling (and the corresponding effect on the yield curve) is captured by the simulations.

4.1 Constant strain rate tests

Figure 7 compares the experimental and simulated stress–strain responses from the constant strain rate tests for both RTM-6 and 736LT. Since the model does not include a failure

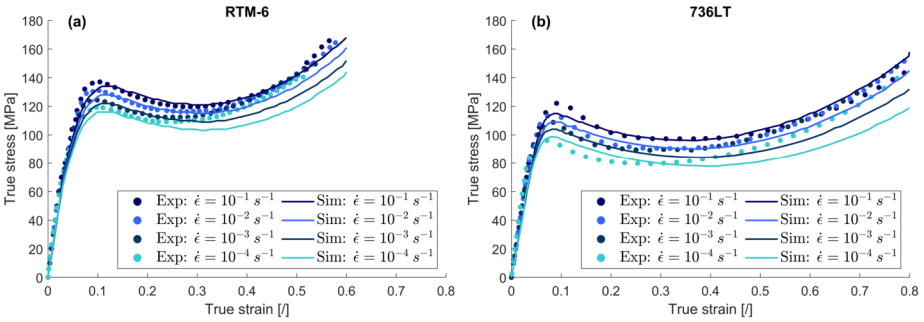


Fig. 7 Comparison of experimental and simulated constant strain rate tests (10^{-1}, 10^{-2}, 10^{-3}, and 10^{-4} s^{-1}) for (a) RTM-6 (data from Morelle 2015) and (b) 736LT. Circles represent experimental data; solid lines denote model predictions. The applied friction coefficient was 0.01 (Color figure online)

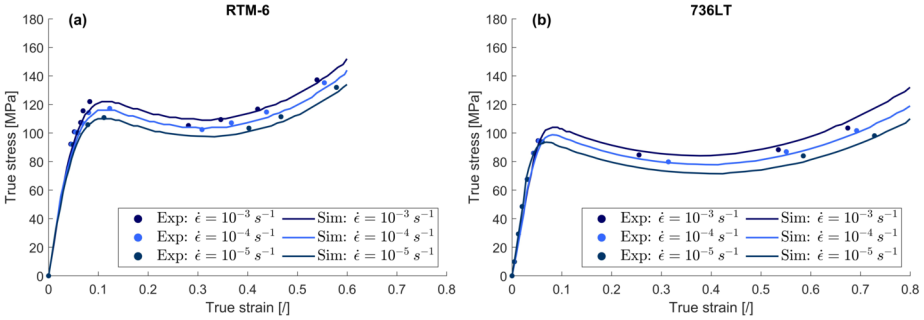


Fig. 8 Apparent true stress as a function of apparent true strain derived from hold-at-load tests and simulations for effective strain rates of 10^{-3}, 10^{-4}, and 10^{-5} s^{-1} for (a) RTM-6 and (b) 736LT. The applied friction coefficient was 0.01 (Color figure online)

criterion, the simulations were terminated near the experimental fracture strains. Overall, the stress–strain behaviour depends approximately linearly on the logarithm of the strain rate, except for the hardening region, which appears largely rate-insensitive.

A good agreement between experimental and simulated results is obtained for both resins, confirming that the fitting procedure successfully captures the rate-dependent yield and softening behaviour. Minor discrepancies remain in the hardening region, where the model slightly underestimates the experimental stresses. For the 736LT resin, the softening region deviates more noticeably at the lowest strain rate (10^{-4} s^{-1}). The data from the hold-at-load creep tests were subsequently converted to equivalent constant strain rate data, using the procedure described in Sect. 2. These converted data correspond to lower effective strain rates, thereby extending the strain rate spectrum accessible for model parameter determination. Figure 8 compares these equivalent stress–strain data with the model predictions.

Interestingly, these additional data points preserve the nearly linear relationship between stress and $\log(\dot{\varepsilon})$, even within the hardening region. One possible explanation for the differences observed between the different tests lies in frictional effects. To evaluate this, simulations were performed with friction coefficients of 0.01 and 0.1. As shown in Fig. 9, increasing the friction coefficient enhances the apparent hardening, as friction suppresses lateral deformation and promotes barreling—an effect also observed by Morelle et al. (2017). By comparing experimental and simulated curves, the effective friction coefficient in the post-

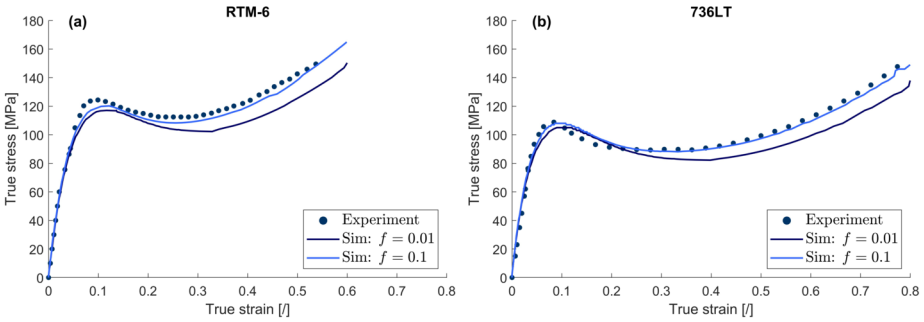


Fig. 9 Comparison between experimental data and simulations for a constant strain rate of 10^{-3} s^{-1} using friction coefficients of 0.01 and 0.1 for (a) RTM-6 (data from Morelle et al. 2017) and (b) 736LT. Circles represent experimental data; solid lines denote model predictions (Color figure online)

yield region is estimated to be close to 0.1, similar to the value of 0.07 reported by Chevalier et al. in the absence of the PTFE film (Chevalier et al. 2016).

One possible cause is that the friction coefficient is rate-dependent. Although it is well known that the friction coefficient of a steel–PTFE interface generally increases with sliding velocity (Dolce et al. 2005; Constantinou et al. 1988), the opposite trend can occur at very low velocities, where a stick–slip mechanism dominates (Dolce et al. 2005; Constantinou et al. 1988; Park et al. 2017). In this regime, the interface remains in near-static contact, and a breakaway or static friction force must be overcome before continuous sliding occurs (Dorafshan et al. 2019; Pleskachevsky and Smurugov 1997). Park et al. reported that for PTFE–steel contacts, stick–slip behaviour arises when the sliding velocity is below approximately 8 mm/min, which applies to all strain rates investigated in this study (Park et al. 2017). Consequently, the higher apparent hardening observed in the CSR tests may partly stem from increased friction at low velocities, which masks the intrinsic strain-rate dependence of the material at large strains. In contrast, the hold-at-load tests are less affected, since the strain rate is inferred from the time derivative of the creep strain, and the initial loading to the target stress was performed at a fixed strain rate of 0.001 s^{-1}. These tests, therefore, provide complementary low-rate information essential for accurately characterising the full viscoplastic response of the material.

4.2 Hold-at-load tests

Figure 10 presents the results of the hold-at-load tests, plotted as strain–time (a, b) and stress–strain (c, d) curves. These results clearly illustrate the dependence of the creep behaviour on the overall strain level. In the pre-yield region, the elongation under constant load remains limited, increasing progressively as the yield point is approached, where the largest creep strains are observed. Beyond yield, the response becomes less sensitive to the applied stress and strain level but exhibits substantially larger total creep strains than in the pre-yield regime.

The highest creep strain rates occur for specimens loaded near the yield point, followed by those tested in the post-yield regime. The model predictions for the strain evolution over time show good agreement with the experiments for both resins. Minor deviations are observed for the 15.8 kN load case of RTM-6 and the 12.4 kN load case of 736LT. These discrepancies arise because, during a hold-at-load test, the model predicts that the upper yield stress eventually drops below the applied true stress. When this occurs, the material

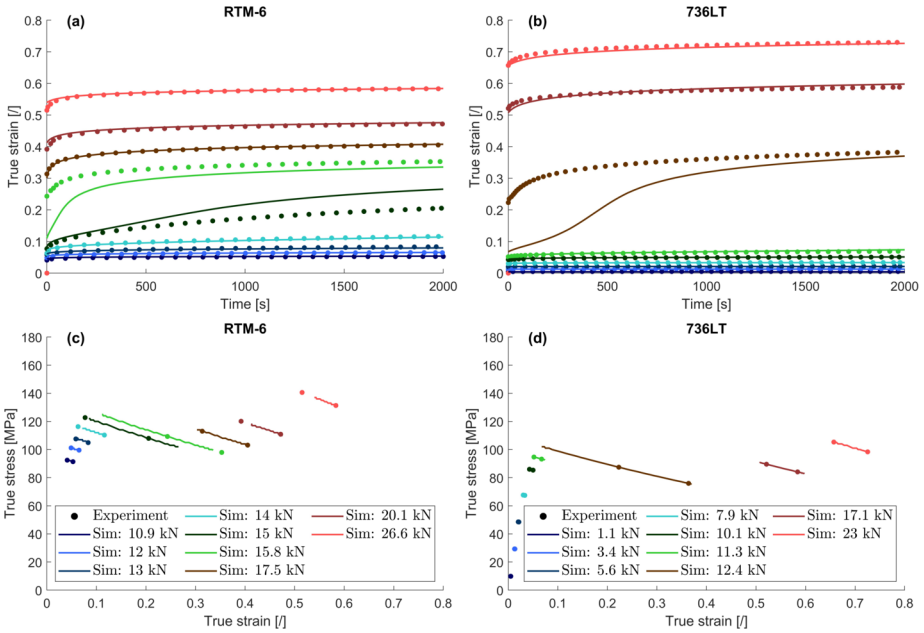


Fig. 10 Results of the hold-at-load tests and model simulations for RTM-6 (a, c) and 736LT (b, d). Panels (a, b) show true strain versus time, while (c, d) show true stress versus true strain. Only the start and end points of the experimental data are indicated (Color figure online)

transitions into the softening regime, producing a sudden increase in strain. Subsequently, as the cross-sectional area of the specimen increases, the true stress decreases, leading to a reduction in the creep rate. This sequence—rapid strain increase followed by a gradual deceleration—marks the transition into the post-yield creep region. The timing of this transition depends on the specific parameters fitted in the rate-dependent hardening law.

The close agreement between the hold-at-load and constant strain rate experiments confirms that the proposed rate-dependent hardening law (Sect. 2) successfully captures the essential physics of the epoxy's time-dependent deformation. In the following sections, additional experiments not used in the calibration are compared with model predictions to further evaluate its predictive capabilities and limitations.

4.3 Long-term hold-at-load test

Figure 11 shows the results of the overnight hold-at-load test, together with the predictions of the proposed model and those of a classical power-law model fitted to the pre-yield data, as described in Sect. 4.2. The creep strain initially increases slowly, followed by a period of accelerated deformation, and finally transitions to a slower rate. The first stage corresponds to the pre-yield region, characterised by a strong stress dependence of the creep rate. The subsequent acceleration occurs once the material enters the softening region, after sufficient deformation time, while the final deceleration is attributed to the increasing cross-sectional area of the specimen as it deforms into the post-yield regime.

The proposed model reproduces both the acceleration and subsequent reduction in creep rate with good accuracy, although it slightly overpredicts the final creep strain for both RTM-6 and 736LT. Based on the long-term trend, it can be expected that the simulations and

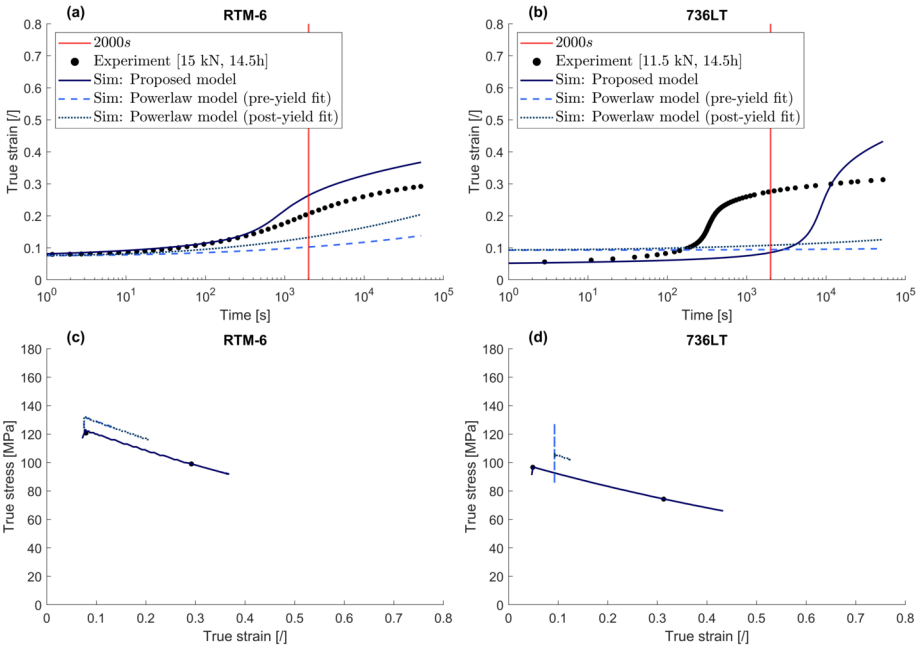


Fig. 11 Results of the long-term hold-at-load test (14.5 hours) for the proposed model, two fitted power-law models (fitted to pre- and post-yield data), and experimental data. The applied load was 15 kN for the RTM-6 resin (adapted from Morelle 2015) (a, c) and 11.5 kN for the 736LT resin (b, d). The red vertical line indicates the 2000-second limit, below which all fitting was performed (Color figure online)

experimental data would eventually converge. For the 736LT resin, the predicted time at which the material crosses the yield point differs from the experiment, reflecting the model's sensitivity to the fitted parameters and the available experimental dataset. Refinement of the calibration procedure could improve the accuracy of this pre- to post-yield transition, which represents the most sensitive region of the model.

A clear difference between the two resins can be observed: the 736LT resin exhibits a sharper and more pronounced increase in strain upon entering the softening regime, consistent with its higher ductility and lower hardening compared to RTM-6 (see Fig. 7). In contrast, the classical power-law model—commonly used in the literature—fails to reproduce this transition. Consequently, extrapolating such power-law fits to longer timescales leads to an underestimation of the creep response, especially near and beyond yield. Furthermore, the power-law predictions are highly sensitive to the time window used for fitting, as shown in Fig. 11: post-yield fits produce higher apparent creep rates than pre-yield fits. In addition, power-law formulations expressed as stress–time relationships do not correctly capture the stress evolution, as seen in Figs. 11c and 11d.

The long-term hold-at-load tests highlight that extrapolating pre-yield data using a simple power-law assumption is inappropriate for predicting the long-term creep behaviour. Since macroscopic tensile specimens typically fail before or around the yield point, traditional tensile creep tests provide limited insight into the full time-dependent behaviour of the resin. Nonetheless, creep behaviour is often inferred from such tests at low stress levels, which tends to underestimate the material's response (Lifshitz and Rotem 1970; Beyerlein et al. 2003; Blassiau et al. 2006; Zhou et al. 2003; Kontou 2011; Ohno et al. 2002; Kawai

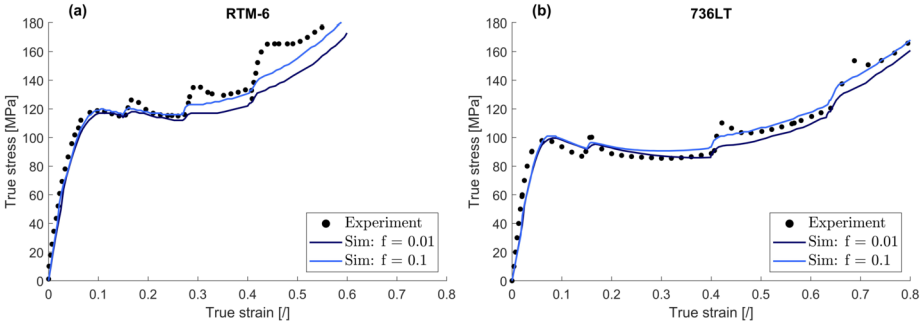


Fig. 12 Strain rate jump tests with experimental data (filled circles) and model predictions (lines). The cross-head displacement velocity was increased stepwise from 0.1 to 1, 10, and 100 mm/min for (a) the RTM-6 resin and (b) the 736LT resin (Color figure online)

1970; Costa and Barros 2015; Feng et al. 2005). In contrast, the current model explicitly incorporates post-yield data, allowing the prediction of the material's long-term response as it evolves from the pre-yield through the softening into the hardening regime. Even so, any extrapolation beyond the experimental range should be undertaken with caution, since the precise transition from pre-yield to post-yield behaviour remains a sensitive aspect of the model (see Fig. 11c and d).

4.4 Strain rate jump test

Figure 12 shows the results of the strain rate jump tests. During these tests, the cross-head displacement rate was increased stepwise, resulting in a corresponding increase in the yield stress at each higher strain rate. Experimentally, a pronounced stress overshoot is observed immediately after each rate jump, after which the material response follows the expected yield curve for the new strain rate. This overshoot can be attributed to the sudden need for additional plastic deformation sites to become active upon a rapid increase in strain rate. The immediate activation of these sites requires additional mechanical energy, leading to a transient stress peak (Morelle 2015).

The current model does not capture these transient overshoots, as it lacks a viscoelastic component dependent on the acceleration of deformation (as it depends only on the rate of deformation). However, it correctly reproduces the overall increase in yield stress with strain rate. The simulations also suggest that a small amount of friction was present during the experiments, despite the use of PTFE films intended to minimise it.

Because the present model does not include a viscoelastic acceleration-dependent component, it cannot reproduce the transient stress rise following a sudden change in strain rate. This limitation implies that the model should be applied with caution when analysing scenarios involving abrupt loading events. In particular, such transient stress surges are expected to play a significant role near fibre breaks, where local strain rates can increase sharply. Incorporating viscoelastic acceleration-dependent effects into the model would therefore be an important direction for future work.

4.5 Cyclic loading test

Figure 13 presents the results of the cyclic compression tests on the epoxy resins. Simulations were performed both with and without friction to assess its influence. The experimental

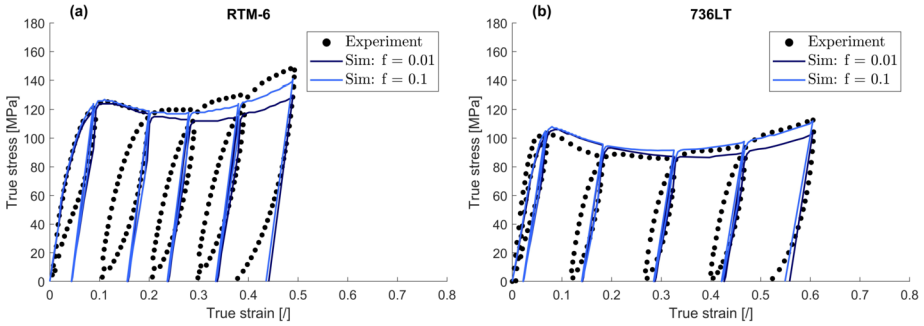


Fig. 13 Cyclic compression tests with experimental data (filled circles) and model predictions (lines) for (a) the RTM-6 resin and (b) the 736LT resin. The cross-head displacement rate was 1 mm/min. Simulations were performed using friction coefficients of 0.01 and 0.1 (Color figure online)

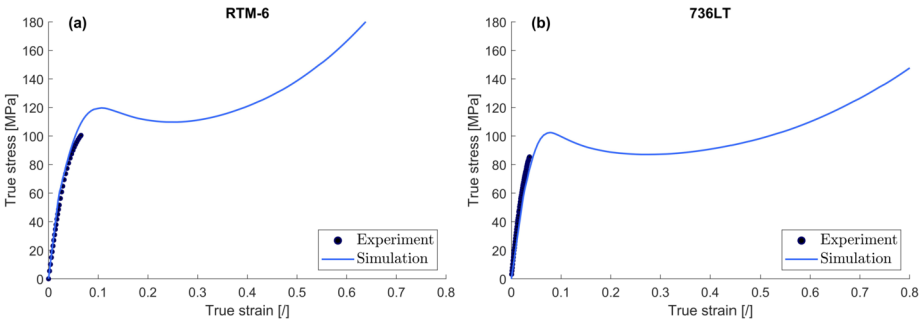


Fig. 14 Tensile experiments and model predictions for (a) the RTM-6 resin (adapted from Morelle et al. 2017) and (b) the 736LT resin. The specimens had a cylindrical geometry (diameter 12 mm) and were tested under a constant cross-head displacement rate of 1 mm/min (Color figure online)

data show a distinct hysteresis upon unloading and reloading, consistent with previous observations in epoxy materials (Morelle 2015; Costa Mattos 2013; Tamrakar et al. 2016). This non-linear unloading behaviour arises from the development of internal back stresses, which can cause backward creep, a purely viscoplastic phenomenon (Chevalier et al. 2018). Since the current plasticity model does not include such back stresses, it cannot reproduce the observed hysteresis during unloading and reloading.

After reloading, the simulated stress–strain response agrees well with the experimental data when friction is included. The post-cyclic yield curve closely matches the monotonic constant strain rate response, showing only minor deviations. This observation is consistent with the findings for DER 353 epoxy resin reported in the literature (Tamrakar et al. 2018), where cyclic loading does not significantly alter the overall yield surface.

Incorporating the non-linear unloading behaviour caused by internal back stresses would improve the predictive capability of the model, but doing so would require a more complex constitutive formulation and additional calibration experiments.

4.6 Tensile test

Figure 14 compares the experimental and simulated stress–strain curves under uniaxial tension. The tensile specimens break before reaching the yield point, a common trend for

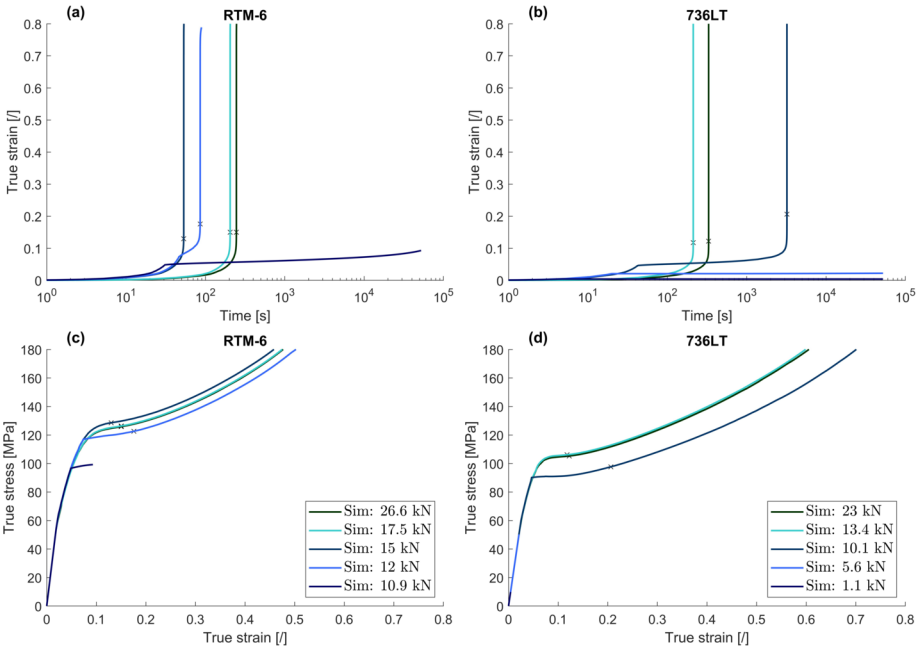


Fig. 15 Tensile creep simulations for (a, c) the RTM-6 resin and (b, d) the 736LT resin under various tensile loads. The cross symbols indicate the point where the true strain rate reached 0.1 s^{-1}, which was used to define the onset of failure. Beyond this point, the strain rate increases rapidly (Color figure online)

macroscopic epoxy resin samples loaded in tension (Morelle et al. 2017; Chevalier et al. 2016; Sui et al. 2019; Zike et al. 2016; Misumi et al. 2016). This premature failure is typically attributed to the presence of critical submicron defects or surface roughness, which act as stress concentrators and trigger brittle fracture (Sui et al. 2019; Rojek et al. 2020; Zike et al. 2016; Misumi et al. 2016).

The model reproduces the tensile response reasonably well, showing slight asymmetry in the non-linear region. However, because the experimental data are limited to strains below the yield point, no definitive conclusions can be drawn regarding the post-yield asymmetry. Further insight could be obtained from small-scale tensile tests on epoxy specimens combined with Digital Image Correlation (DIC) techniques, which would enable accurate characterisation of the local strain fields and post-yield behaviour (Hobbiebrunken et al. 2007; Misumi et al. 2016; Poulain et al. 2014; Littell et al. 2008). The proposed hardening law could then be readily extended to include tension–compression asymmetry or pressure dependence through an appropriate yield criterion, such as the Drucker–Prager model.

4.7 Creep behaviour in tension

Figure 15 presents the simulation results obtained using the tensile specimen geometry described in Sect. 3.7, with a constant cross-head displacement rate of 10 mm/min. The onset of failure was identified at the point where the true strain rate reached 0.1 s^{-1}, as beyond this value the strain rate increases rapidly, indicating the imminent onset of catastrophic failure.

A defect-free cylindrical epoxy specimen subjected to a sustained tensile load is expected to exhibit the three classical creep stages—primary, secondary, and tertiary (Nechad et al.

2005; Vujosevic and Krajcinovic 1997). The simulations reproduce this behaviour: an initial transient (primary) stage with decreasing strain rate, followed by a quasi-steady-state (secondary) region, and finally a rapid acceleration (tertiary stage) associated with local necking and reduction of the cross-sectional area. The 12 kN and 10.1 kN load cases for RTM-6 and 736LT, respectively, clearly illustrate these three stages. The predicted time to failure (marked by a cross symbol) depends on both the applied load and the strain accumulated before loading.

At lower load levels, such as 1.1 kN and 5.6 kN for 736LT and 10.9 kN for RTM-6, only the primary and secondary creep stages are observed within the simulated time window. Nonetheless, given sufficient time, the tertiary stage would eventually be reached, leading to specimen failure. Conversely, for higher loads (15 kN, 17.5 kN, and 26.6 kN for RTM-6, and 13.4 kN and 23 kN for 736LT), the primary stage transitions almost immediately into tertiary failure, consistent with the expected stress dependence of creep rupture.

Experimental validation of these tensile creep simulations is challenging, as bulk epoxy specimens typically fail in a brittle manner before significant plastic deformation occurs (Morelle et al. 2017; Chevalier et al. 2016; Sui et al. 2019; Zike et al. 2016; Misumi et al. 2016). Bulk and surface defects often promote early failure, limiting experimental access to the post-yield regime. In principle, tensile creep experiments on micron-scale epoxy fibres—where much higher strains can be achieved—would provide an ideal validation dataset, but such data is, to the best of the authors' knowledge, not yet available.

Nonetheless, existing tensile creep studies on macroscopic specimens at lower stress levels report trends consistent with the present model predictions: even when loaded below the macroscopic yield stress, epoxy resins gradually enter the softening regime over time (Perrella et al. 2019; Feng et al. 2005). This behaviour is well captured by the current model, as illustrated for the 1.1 kN case of the 736LT resin (Fig. 15d). Moreover, Costa and Barros (2015) showed that epoxy loaded in tension at approximately 60% of its macroscopic tensile strength exhibits a linear viscoelastic–viscoplastic response and can reach creep strains exceeding twice the nominal failure strain. These findings support the central assumption of this work—that significant viscoplastic deformation can occur in tension, even when not directly observable in conventional macroscopic constant strain rate tests.

In summary, the simulations capture the characteristic primary, secondary, and tertiary creep stages under tensile loading, consistent with theoretical expectations and available experimental evidence. However, further experimental validation under controlled tensile creep conditions would be required to fully confirm the model's predictive capability in this loading regime.

5 Conclusions and outlook

The primary goal of this study was to develop a resin model capable of capturing the subtle time-dependent response of epoxy resins, both in the pre-yield and post-yield regimes—regions that are critical for accurately describing stress redistribution near fibre breaks. A second objective was to design a model that can be easily implemented in continuum-scale simulations and finite element (FE) codes. Finally, the resin characterisation procedure was deliberately kept simple, relying on standard tests available in most mechanical laboratories. These included compression tests on cylindrical specimens under constant strain rate and hold-at-load creep conditions. Using three to four specimens across strain rates allowed the determination of the yield surface shape and its rate dependence at higher strain rates, while several short hold-at-load tests (on the order of 2000 s) near and beyond yield provided the

rate dependence at the lower end of the strain-rate spectrum. Longer holds naturally probe lower equivalent strain rates. Hold-at-load tests at low stress levels, such as those performed for the 736LT resin, were found to contribute little to parameter fitting and may be omitted in future characterisation efforts.

This work introduces a unified, rate-dependent hardening law that effectively captures the complex, time-dependent behaviour of highly crosslinked epoxies and other glassy polymers over a wide range of loading conditions. Calibrated using both constant strain rate and hold-at-load data for RTM-6 (from literature Morelle 2015) and for 736LT epoxies (new experiments), the model demonstrates robust predictive capability across multiple scenarios, including long-term creep, stress relaxation, cyclic loading, and abrupt strain-rate jumps. Implemented in the FE code Abaqus through a user-defined Fortran subroutine, the model provides a practical, computationally efficient framework for simulating resin viscoplasticity in fibre-reinforced composites.

Some limitations remain. The current model does not include viscoelasticity or back stresses, and should therefore be used with care in cases involving unloading, strain reversal, or abrupt transients. These "transitional" effects—observed, for example, during sudden strain-rate changes—are not fully captured. However, the overall yield curve is well reproduced once steady conditions are reached (Fig. 12). Under smooth loading, such as slow cyclic deformation, the model accurately reproduces the experimental response (Fig. 13). Consequently, it is well suited for modelling creep and relaxation phenomena around fibre breaks, but less appropriate for situations involving significant kinematic hardening or complex load reversals. Likewise, tensile and shear loading should be interpreted cautiously, as the asymmetry of the yield locus remains uncertain due to the limited availability of tensile data at large strains. For both RTM-6 and 736LT, this asymmetry appears modest in the pre-yield region (Morelle et al. 2017). Future studies could extend the model to asymmetric yielding by incorporating additional tensile and torsional data from small-scale specimens that avoid premature failure (Hobbiebrunken et al. 2007; Misumi et al. 2016; Littell et al. 2008). Another challenge is the absence of an explicit failure criterion, which ideally should include a volume-dependent term (Littell et al. 2008; Misumi et al. 2016; Zike et al. 2016).

Comparison between the two resins reveals that RTM-6 exhibits a slightly higher yield strength (140 MPa at $\dot{\epsilon} = 10^{-1}$ s^{-1}) than 736LT (122 MPa at the same rate), but the latter shows greater ductility, with a true strain at failure of approximately 0.8 versus 0.6 for RTM-6. The RTM-6 resin also displays somewhat stronger hardening. Although both resins exhibit similar time-dependent behaviour, the 736LT resin shows a more pronounced "sudden" creep acceleration when crossing the yield point, followed by a plateau in the post-yield regime. This behaviour could be beneficial for stress redistribution in composites: under sustained loading, existing fibre breaks could relax local stresses over time, potentially delaying the formation of critical fibre clusters upon reloading.

Further exploration of the temperature dependence of the hardening law would allow the use of time–temperature superposition to extend predictions to longer timescales (Nakada and Miyano 2013; Tamrakar et al. 2019; Tsugiyuki et al. 2013; Barbero 2011; Papanicolaou and Zaoutsos 2011). The framework could also be adapted for other matrix materials such as amorphous thermoplastics, where the relative contributions to the hardening law would differ owing to the absence of chemical crosslinks. As many key mechanical properties of epoxies scale with the glass transition temperature (T_g) (Klavzer et al. 2025), future work could establish correlations between model coefficients and T_g, enabling fast generalisation of parameters with minimal experimental effort.

Overall, the proposed rate-dependent hardening law offers a simple yet powerful tool for efficient finite element simulations of time-dependent epoxy behaviour. Its computational

robustness makes it well suited for multi-scale analyses and applications such as fibre-break models (Swolfs et al. 2015), ultimately contributing to improved lifetime prediction of unidirectional composite structures, including pressure vessels and wind turbine blades, where matrix viscoplasticity plays a decisive role.

Author contributions Vincent Feyen: Conceptualization, Data curation, Methodology, Software, Investigation, Writing - Original Draft. Christian Breite: Investigation, Writing - Review & Editing, Supervision. Jérémy Chevalier: Data curation, Writing - Review & Editing, Supervision. Thomas Pardoen: Writing - Review & Editing, Supervision. Yentl Swolfs: Writing - Review & Editing, Resources, Supervision.

Funding information The research leading to these results has been conducted in the framework of the FiBreMoD project and has received funding from the European Union's Horizon 2020 research and innovation programme under the Marie Skłodowska-Curie grant agreement No. 722626.

Data availability All codes required to reproduce these findings are available to download from Mendeley data (Feyen et al. 2024).

Materials availability Not applicable.

Code availability All codes required to reproduce these findings are available to download from Mendeley data (Feyen et al. 2024).

Declarations

Ethics approval and consent to participate Not applicable.

Consent for publication All authors have read and approved the final version of the manuscript and consent to its submission for publication in this journal. Where applicable, consent has also been obtained from individuals involved in the study or from their legal guardians.

Declaration of generative AI and AI-assisted technologies in the writing process During the preparation of this work, the authors used chatGPT to improve its readability. After using this tool/service, the authors reviewed and edited the content as needed and take full responsibility for the content of the published article.

Competing interests The authors declare no competing interests.

References

ASTM: Standard Test Method for Compressive Properties of Rigid Plastics (D695-15) (2015). https://doi.org/10.1520/D0695-15. www.astm.org

Barbero, E.J.: Time-temperature-age superposition principle for predicting long-term response of linear viscoelastic materials. In: Creep and Fatigue in Polymer Matrix Composites (2011)

Beyerlein, I.J., Phoenix, S.L., Raj, R.: Time evolution of stress redistribution around multiple fiber breaks in a composite with viscous and viscoelastic matrices. Int. J. Solids Struct. **35**, 3177–3211 (1998). https://doi.org/10.1016/S0020-7683(98)00010-9

Beyerlein, I.J., Zhou, C.H., Schadler, L.S.: A time dependent micro-mechanical fiber composite model for inelastic zone growth in viscoelastic matrices. Mater. Sci. **40**, 2171–2194 (2003). https://doi.org/10.1016/S0020-7683/03/

Blassiau, S., Thionnet, A., Bunsell, A.R.: Micromechanisms of load transfer in a unidirectional carbon fibre-reinforced epoxy composite due to fibre failures. Part 2: influence of viscoelastic and plastic matrices on the mechanisms of load transfer. Compos. Struct. **74**, 319–331 (2006). https://doi.org/10.1016/j.compstruct.2005.04.029

Chevalier, J., Morelle, X.P., Bailly, C., Camanho, P.P., Pardoen, T., Lani, F.: Micro-mechanics based pressure dependent failure model for highly cross-linked epoxy resins. Eng. Fract. Mech. **158**, 1–12 (2016). https://doi.org/10.1016/j.engfracmech.2016.02.039

Chevalier, J., Brassart, L., Lani, F., Bailly, C., Pardoen, T., Morelle, X.P.: Unveiling the nanoscale heterogeneity controlled deformation of thermosets. J. Mech. Phys. Solids **121**, 432–446 (2018). https://doi.org/10.1016/j.jmps.2018.08.014

Cole, D.P., Henry, T.C., Gardea, F., Haynes, R.A.: Interphase mechanical behavior of carbon fiber reinforced polymer exposed to cyclic loading. Compos. Sci. Technol. **151**, 202–210 (2017). https://doi.org/10.1016/j.compscitech.2017.08.012

Constantinou, M., Reinhorn, A., Watson, R.: Teflon bearings in aseismic base isolation: experimental studies. **147**, 9–13 (1988)

Costa Mattos, H.S.: Plastic behaviour of an epoxy polymer under cyclic tension. Polym. Test. **32**, 1–8 (2013). https://doi.org/10.1016/j.polymertesting.2012.08.009

Costa, I., Barros, J.: Tensile creep of a structural epoxy adhesive: experimental and analytical characterization. Int. J. Adhes. Adhes. **59**, 115–124 (2015). https://doi.org/10.1016/j.ijadhadh.2015.02.006

Dolce, M., Cardone, D., Croatto, F.: Frictional behavior of steel-ptfe interfaces for seismic isolation. Bull. Earthq. Eng. **3**(1), 75–99 (2005). https://doi.org/10.1007/s10518-005-0187-9

Dorafshan, S., Johnson, K.R., Maguire, M., Halling, M.W., Barr, P.J., Culmo, M.: Friction coefficients for slide-in bridge construction using ptfe and steel sliding bearings. J. Bridge Eng. **24**(6) (2019). https://doi.org/10.1061/(asce)be.1943-5592.0001417

Du, Z.Z., McMeeking, R.M.: Creep models for metal matrix composites with long brittle fibers. J. Mech. Phys. Solids **43**, 701–726 (1985)

Feng, C.-W., Keong, C.-W., Hsueh, Y.-P., Wang, Y.-Y., Sue, H.-J.: Modeling of long-term creep behavior of structural epoxy adhesives. Int. J. Adhes. Adhes. **25**(5), 427–436 (2005). https://doi.org/10.1016/j.ijadhadh.2004.11.009

Feyen, V., Breite, C., Swolfs, Y.: Epoxy Constitutive Creep Subroutine Model (Abaqus). Mendeley Data, v1 (2024). https://doi.org/10.17632/jrf277r82n.1

Fiedler, B., Hojo, M., Ochiai, S., Schulte, K., Ando, M.: Failure behavior of an epoxy matrix under different kinds of static loading. Compos. Sci. Technol. **61**(11), 1615–1624 (2001). https://doi.org/10.1016/s0266-3538(01)00057-4

Foreman, J.P., Porter, D., Behzadi, S., Jones, F.R.: A model for the prediction of structure property relations in cross-linked polymers. Polymer **49**, 5588–5595 (2008). https://doi.org/10.1016/j.polymer.2008.09.034

Gerritzen, J., Müller-Pabel, M., Müller, J., Gröger, B., Lorenz, N., Hopmann, C., Gude, M.: Development of a high-fidelity framework to describe the process-dependent viscoelasticity of a fast-curing epoxy matrix resin including testing, modelling, calibration and validation. Polymers **14**(17), 3647 (2022). https://doi.org/10.3390/polym14173647

Goertzen, W.K., Kessler, M.R.: Creep behavior of carbon fiber/epoxy matrix composites. Mater. Sci. Eng. **421**, 217–225 (2006). https://doi.org/10.1016/j.msea.2006.01.063

Heuvel, P.W.J., Wubbolts, M.K., Young, R.J., Peijs, T.: Failure phenomena in two-dimensional multi-fibre model composites: 5. A finite element study. Composites, Part A **513**, 1121–1135 (1998)

Hobbiebrunken, T., Fiedler, B., Hojo, M., Tanaka, M.: Experimental determination of the true epoxy resin strength using micro-scaled specimens. Composites, Part A **38**, 814–818 (2007). https://doi.org/10.1016/j.compositesa.2006.08.006

Hsieh, T.H., Kinloch, A.J., Masania, K., Taylor, A.C., Sprenger, S.: The mechanisms and mechanics of the toughening of epoxy polymers modified with silica nanoparticles. Polymer **51**, 6284–6294 (2010). https://doi.org/10.1016/j.polymer.2010.10.048

Ilioni, A., Badulescu, C., Carrere, N., Davies, P., Thévenet, D.: A viscoelastic-viscoplastic model to describe creep and strain rate effects on the mechanical behaviour of adhesively-bonded assemblies. Int. J. Adhes. Adhes. **82**, 184–195 (2018). https://doi.org/10.1016/j.ijadhadh.2017.12.003

Iyengar, N., Curtin, W.A.: Time-dependent failure in fiber-reinforced composites by matrix and interface shear creep. Acta Metall. **45**, 3419 (1997)

Jianlin, Z., Rui, R., Ziruo, T., Jie, R., Changfang, Z.: Analysis of nonlinear mechanical behavior of resin materials at low and medium strain rates. Polym. Compos. **43**(6), 3699–3707 (2022). https://doi.org/10.1002/pc.26647

Kawai, M.: Constitutive modeling of viscoplastic deformation of polymer matrix composites. In: Creep and Fatigue in Polymer Matrix Composites (1970)

Kelly, K.W., Barbero, E.: The effect of fiber damage on the longitudinal creep of a cfmmc. Int. J. Solids Struct. **30**, 3417–3429 (1993). https://doi.org/10.1016/0020-7683(93)90091-K

Klavzer, N., Chevalier, J., Breite, C., Morelle, X.P., Swolfs, Y., Pardoen, T.: Master trends in the elasto-viscoplastic behaviour of highly cross-linked epoxy resins. Mech. Time-Depend. Mater. **29**(3) (2025). https://doi.org/10.1007/s11043-025-09804-w

Kontou, E.: Creep Analysis of Polymer Matrix Composites Using Viscoplastic Models, pp. 273–301. Elsevier (2011). https://doi.org/10.1533/9780857090430.1.273

Kotelnikova-Weiler, N., Baverel, O., Ducoulombier, N., Caron, J.-F.: Progressive damage of a unidirectional composite with a viscoelastic matrix, observations and modelling. Compos. Struct. (2017). https://doi.org/10.1016/j.compstruct.2017.12.067

Koyanagi, J., Hatta, H., Ogawa, F., Kawada, H.: Time-dependent reduction of tensile strength caused by interfacial degradation under constant strain duration in ud-cfrp. J. Compos. Mater. **41**(25), 3007–3026 (2007). https://doi.org/10.1177/0021998307082175

Krauklis, A.E., Akulichev, A.G., Gagani, A.I., Echtermeyer, A.T.: Time–temperature–plasticization superposition principle: predicting creep of a plasticized epoxy. Polymers **11**(11), 1848 (2019). https://doi.org/10.3390/polym11111848

Kumar, R.S., Talreja, R.: A continuum damage model for linear viscoelastic composite materials. Mech. Mater. **35**, 463–480 (2003)

Kumar, S., Sahay, S.R., Singh, S.S., Rozycki, P.: Exploring the filler morphology and temperature-dependent compressive response of glass-filled epoxy composites: insights from experiments and viscoplastic simulations. Polym. Compos. **45**(18), 17001–17016 (2024). https://doi.org/10.1002/pc.28946

Lagoudas, D.C., Chung-Yuen, H., Phoenix, S.L.: Time evolution of overstress profiles near broken fibers in a composite with a viscoelastic matrix. Int. J. Solids Struct. **25**(1), 45–66 (1989). https://doi.org/10.1016/0020-7683(89)90103-0

Lifshitz, J.M., Rotem, A.: Time-dependent longitudinal strength of unidirectional fibrous composites*. Science **44**, 61052–61068 (1970)

Littell, J.D., Ruggeri, C.R., Goldberg, R.K., Roberts, G.D., Arnold, W.A., Binienda, W.K.: Measurement of epoxy resin tension, compression, and shear stress–strain curves over a wide range of strain rates using small test specimens. J. Aerosp. Eng. **21**(3), 162–173 (2008). https://doi.org/10.1061/(asce)0893-1321(2008)21:3(162)

Liu, C., Xu, F., Jiang, Z., Guo, H., Wen, J., Li, J.: A viscoelastic-viscoplastic constitutive model for nanoparticle-reinforced epoxy composites: particle, temperature, and strain rate effects. Mater. Today Commun. **33**, 104849 (2022). https://doi.org/10.1016/j.mtcomm.2022.104849

Mair, G.W.: Safety Assessment of Composite Cylinders for Gas Storage by Statistical Methods. Springer (2017)

Mason, D.D., Chung-Yuen, H., Phoenix, S.L.: Stress profiles around a fiber break in a composite with a nonlinear, power law creeping matrix. Int. J. Solids Struct. **29**(23), 2829–2854 (1992). https://doi.org/10.1016/0020-7683(92)90143-h

Misumi, J., Ganesh, R., Sockalingam, S.: Experimental characterization of tensile properties of epoxy resin by using micro-fiber specimens. J. Reinf. Plast. Compos. **0**, 1–10 (2016). https://doi.org/10.1177/0731684416669248

Miyake, T.: Measuring Fiber Strain and Creep Behavior in Polymer Matrix Composites Using Raman Spectroscopy, pp. 149–183. Elsevier (2011). https://doi.org/10.1533/9780857090430.1.149

Morelle, X.: Mechanical characterization and physics-based modeling of highly-crosslinked epoxy resin (2015)

Morelle, X.P., Chevalier, J., Bailly, C., Pardoen, T., Lani, F.: Mechanical characterization and modeling of the deformation and failure of the highly crosslinked rtm6 epoxy resin. Mech. Time-Depend. Mater. **21**, 419–454 (2017). https://doi.org/10.1007/s11043-016-9336-6

Nakada, M., Miyano, Y.: Advanced accelerated testing methodology for long-term life prediction of cfrp laminates. J. Compos. Mater. **49**(2), 163–175 (2013). https://doi.org/10.1177/0021998313515019

Nechad, H., Helmstetter, A., Guerjouma, R.E., Sornette, D.: Andrade and critical time-to-failure laws in fiber-matrix composites: experiments and model. J. Mech. Phys. Solids **53**, 1099–1127 (2005). https://doi.org/10.1016/j.jmps.2004.12.001

Neogi, A.: Cavitation in epoxies under composite-like stress states. Composites, Part A **106**, 52–58 (2018). https://doi.org/10.1016/j.compositesa.2017.12.003

Nguyen, V.-D., Lani, F., Pardoen, T., Morelle, X.P., Noels, L.: A large strain hyperelastic viscoelastic-viscoplastic-damage constitutive model based on a multi-mechanism non-local damage continuum for amorphous glassy polymers. Int. J. Solids Struct. **96**, 192–216 (2016). https://doi.org/10.1016/j.ijsolstr.2016.06.008

NTPT Thinpreg 736LT Datasheet (2017)

Ohno, N., Miyake, T.: Stress relaxation in broken fibers in unidirectional composites: modeling and application to creep rupture analysis. Int. J. Plast. **15**, 23 (1999)

Ohno, N., Ando, T., Miyake, T., Biwa, S.: A variational method for unidirectional fiber-reinforced composites with matrix creep. Int. J. Solids Struct. **39**(39), 159 (2002)

Okabe, T., Nishikawa, M., Takeda, N.: Micromechanics on the rate-dependent fracture of discontinuous fiber-reinforced plastics. Int. J. Damage Mech. **19**, 339 (2010). https://doi.org/10.1177/1056789509103649

Papanicolaou, G.C., Zaoutsos, S.P.: Viscoelastic constitutive modeling of creep and stress relaxation in polymers and polymer matrix composites. In: Creep and Fatigue in Polymer Matrix Composites (2011)

Park, J.S., Lee, S.M., Joo, B.S., Jang, H.: The effect of material properties on the stick–slip behavior of polymers: a case study with pmma, pc, ptfe, and pvc. Wear **378–379**, 11–16 (2017). https://doi.org/10.1016/j.wear.2017.01.097

Paul, S., Singh, S.S.: Modeling the strain-softening behavior of glass-filled epoxy composites using a hyperelastic–viscoplastic model. Mech. Time-Depend. Mater. **27**(3), 929–947 (2022). https://doi.org/10.1007/s11043-022-09574-9

Perrella, M., Berardi, V.P., Cricrì, G., Esposito, R.: Experimental evaluation of the long-term creep deformations of epoxy resin. Procedia Struct. Integr. **24**, 601–611 (2019). https://doi.org/10.1016/j.prostr.2020.02.053

Perreux, D., Thiebaud, F.: Continuum damage mechanical modeling of creep damage and fatigue in polymer matrix composites. In: Creep and Fatigue in Polymer Matrix Composites (2011)

Phoenix, S.L., Schwartz, P., Robinson, H.H. IV: Statistics for the strength and lifetime in creep-rupture of model carbon/epoxy composites. Compos. Sci. Technol. **32**, 81–120 (1988)

Pleskachevsky, Y.M., Smurugov, V.A.: Thermal fluctuations at ptfe friction and transfer. Wear **209**(1–2), 123–127 (1997). https://doi.org/10.1016/s0043-1648(97)00034-3

Poulain, X., Benzerga, A.A., Goldberg, R.K.: Finite-strain elasto-viscoplastic behavior of an epoxy resin: experiments and modeling in the glassy regime. Int. J. Plast. **62**, 138–161 (2014). https://doi.org/10.1016/j.ijplas.2014.07.002

Rojek, J., Breite, C., Swolfs, Y., Laiarinandrasana, L.: Void growth measurement and modelling in a thermosetting epoxy resin using sem and tomography techniques. Contin. Mech. Thermodyn. **32**(2), 471–488 (2020). https://doi.org/10.1007/s00161-020-00865-5

Rosen, B.W.: Tensile failure of fibrous composites. AIAA J. **7** (1964)

Schadler, L.S., Amer, M.S., Iskandarani, B.: Experimental measurement of fiber/fiber interaction using micro Raman spectroscopy. Mech. Mater. **23**, 205–216 (1996)

Scott, A.E., Mavrogordato, M., Wright, P., Sinclair, I., Spearing, S.M.: In situ fibre fracture measurement in carbon epoxy laminates using high resolution computed tomography. Compos. Sci. Technol. **71**, 1471–1477 (2011). https://doi.org/10.1016/j.compscitech.2011.06.004

Silva, P., Valente, T., Azenha, M., Sena-Cruz, J., Barros, J.: Viscoelastic response of an epoxy adhesive for construction since its early ages: experiments and modelling. Composites, Part B **116**, 266–277 (2017). https://doi.org/10.1016/j.compositesb.2016.10.047

Smith, M.: ABAQUS/Standard User's Manual, Version 6.9. Dassault Systèmes Simulia Corp, United States (2009)

Sui, X.M., Tiwari, M., Greenfeld, I., Khalfin, R.L., Meeuw, H., Fiedler, B., Wagner, H.D.: Extreme scale-dependent tensile properties of epoxy fibers. eXPRESS Polym. Lett. **13**(11), 993–1003 (2019). https://doi.org/10.3144/expresspolymlett.2019.86

Swolfs, Y., McMeeking, R.M., Verpoest, I., Gorbatikh, L.: Matrix cracks around fibre breaks and their effect on stress redistribution and failure development in unidirectional composites. Compos. Sci. Technol. **108**, 16–22 (2015). https://doi.org/10.1016/j.compscitech.2015.01.002

Systemes: Abaqus user subroutine: CREEP (2023). https://help.3ds.com/2023/english/dssimulia_established/SIMACAESUBRefMap/simasub-c-creep.htm?contextscope=all#simasub-c-creep. Accessed 03-09-2024

Tamrakar, S., Gama Haque, B.Z., Gillespie, J.W.: High rate test method for fiber-matrix interface characterization. Polym. Test. **52**, 174–183 (2016). https://doi.org/10.1016/j.polymertesting.2016.04.016

Tamrakar, S., Ganesh, R., Sockalingam, S., Haque, B.Z., Gillespie, J.W.: Experimental investigation of strain rate and temperature dependent response of an epoxy resin undergoing large deformation. J. Dyn. Behav. Mater. **4**(1), 114–128 (2018). https://doi.org/10.1007/s40870-018-0144-8

Tamrakar, S., Ganesh, R., Sockalingam, S., Haque, B.Z.G., Gillespie, J.W.: Strain rate-dependent large deformation inelastic behavior of an epoxy resin. J. Compos. Mater. **54**(1), 71–87 (2019). https://doi.org/10.1177/0021998319859054

Thionnet, A., Chou, H.Y., Bunsell, A.: Fibre break processes in unidirectional composites. Composites, Part A **65**, 148–160 (2014). https://doi.org/10.1016/j.compositesa.2014.06.009

Tsugiyuki, O., Nakada, M., Miyano, Y.: Temperature dependence of longitudinal tensile strength in unidirectional carbon fiber-reinforced plastic. J. Compos. Mater. **48**(28), 3569–3573 (2013). https://doi.org/10.1177/0021998313512349

Verschatse, O., Daelemans, L., Van Paepegem, W., De Clerck, K.: In-situ observations of microscale ductility in a quasi-brittle bulk scale epoxy. Polymers **12**(11), 2581 (2020). https://doi.org/10.3390/polym12112581

Vujosevic, M., Krajcinovic, D.: Creep rupture of polymers-a statistical model. Int. J. Solids Struct. **34**, 1105–1122 (1997). https://doi.org/10.1016/S0020-7683(96)00067-4

Zhang, L., Klimm, W.J., Kwok, K., Yu, W.: A nonlinear viscoelastic-viscoplastic constitutive model for epoxy polymers. In: AIAA SCITECH 2022 Forum. American Institute of Aeronautics and Astronautics (2022). https://doi.org/10.2514/6.2022-1120

Zhou, C.H., Schadler, L.S., Beyerlein, I.J.: Time-dependent micromechanical behavior in graphite/epoxy composites under constant load: a combined experimental and theoretical study. Acta Mater. **50**, 365–377 (2002)

Zhou, C.H., Schadler, L.S., Beyerlein, I.J.: Stress concentrations in graphite/epoxy model composites during creep at room temperature and elevated temperatures. Mater. Sci. **38** (2003)

Zike, S., Sørensen, B.F., Mikkelsen, L.P.: Experimental determination of the micro-scale strength and stress-strain relation of an epoxy resin. Mater. Des. **98**, 47–60 (2016). https://doi.org/10.1016/j.matdes.2016.02.102

Publisher's note Springer Nature remains neutral with regard to jurisdictional claims in published maps and institutional affiliations.

Springer Nature or its licensor (e.g. a society or other partner) holds exclusive rights to this article under a publishing agreement with the author(s) or other rightsholder(s); author self-archiving of the accepted manuscript version of this article is solely governed by the terms of such publishing agreement and applicable law.